Measurements on a yawed rotor blade pitching in reverse flow

Luke R. Smith and Anya R. Jones

Phys. Rev. Fluids **4**, 034703 — Published 12 March 2019

DOI: 10.1103/PhysRevFluids.4.034703

Measurements on a Yawed Rotor Blade Pitching in Reverse Flow

Luke R. Smith* and Anya R. Jones†
University of Maryland, College Park
(Dated: February 8, 2019)

In forward flight, high advance ratio rotors encounter a large region of reverse flow on their retreating side. The reverse flow region is the cause of significant separation in sharp-trailing edge rotor blades and is believed to be dominated by a flow structure called the reverse flow dynamic stall vortex (RFDSV). This vortex incurs large, unsteady torsional loads that are not well-predicted by modern comprehensive rotorcraft codes. To gain a physical understanding of the impact of yaw on the RFDSV, a sub-scale, NACA0012 model rotor blade has been experimentally tested at two reverse flow yaw angles, $\Lambda_{\text{rev}} = 0^\circ$ (unyawed) and $\Lambda_{\text{rev}} = 30^\circ$ (yawed), over a range of reduced frequencies, $0.160 < k < 0.450$. Pressure time histories were obtained from surface-mounted unsteady pressure transducers, and three-component velocity fields were obtained using stereoscopic particle image velocimetry at the midspan. The present work focuses on the impact of yaw on the strength, number, and behavior of vortices shed for a given set of pitch kinematics. In cases where the unyawed blade shed multiple vortices, the presence of yaw was found to suppress secondary flow structures, including the trailing-edge vortex, and thus delay the breakup of the RFDSV to later times in the pitch cycle. The suppression of secondary flow structures was consistent across multiple kinematic scalings of the flowfield, suggesting that the flow at $\Lambda_{\text{rev}} = 30^\circ$ is subject to physical mechanisms not present at $\Lambda_{\text{rev}} = 0^\circ$. This work proposes that spanwise flow, which was found to substantially increase at $\Lambda_{\text{rev}} = 30^\circ$, amplifies small spanwise vorticity gradients in the flowfield and results in the net transport of vorticity along the blade span. The transport of vorticity, particularly in 3D flows, is the subject of ongoing experimental efforts, and the current work represents a first step in understanding its role in reverse flow aerodynamics.

I. INTRODUCTION

High speed helicopters have considerable military and commercial application [1, 2], but aerodynamic limitations in forward flight prevent their widespread design and development. One such limitation is a region of reverse flow, or flow traveling from a rotor blade's geometric trailing edge to its geometric leading edge, on the retreating side of the rotor. Illustrated in Figure 1a, reverse flow occurs in regions of a rotor disk where the forward flight speed of the helicopter surpasses the rotational velocity of the rotor blades. The size of this region scales directly with the helicopter's advance ratio (μ), defined in Equation 1.

$$\mu = \frac{V_\infty}{\Omega R} \tag{1}$$

The numerator in Equation 1 represents the forward flight speed of the helicopter, while the denominator represents the rotor tip speed. Substantial reverse flow is in turn present in high-speed designs, where cruise velocity is large, and in low power, or "slowed rotor," designs, where the rotor angular velocity is low. The aerodynamics of reverse flow are characterized by downward-acting lift, high drag, and unsteady shifts in the center of pressure of each rotor blade. These unsteady effects have a detrimental impact on rotor blade dynamics at high advance ratio, and their effect on unsteady loading is unable to be accurately predicted by modern rotorcraft design tools [3, 4]. The current work is part of an ongoing experimental effort to gain a physical understanding of unsteady forces in a helicopter rotor's reverse flow region, with the ultimate goal of improving load predictions for designs with significant reverse flow.

Prior experimental work has sought to identify which unsteady features in reverse flow are most critical to a low-order aerodynamics model. The reverse flow dynamic stall vortex (RFDSV), a flow structure present in full-scale [6] and Mach-scale rotor experiments [7], has emerged as a particularly important feature of the region and is believed to impart large, unsteady torsional loads on blades passing through reverse flow. A successful low-order model will require a physical understanding of how the various sources of unsteadiness on a rotor, including a time-varying freestream, dynamically pitching blades, and time-varying radial flow, influence the behavior and shedding pattern of this vortex. Previous experimental efforts by the authors have characterized the RFDSV in sinusoidal [8] and linear pitching [9] but have been limited to 2D experiments at constant freestream. The purpose of this work is to begin investigating three dimensional effects by introducing a static yaw angle to a pitching airfoil in reverse flow.

The yaw angle of a blade element, defined as the angle between the local velocity vector and the airfoil chord line, is effectively a measure of the degree of radial flow at a position on the rotor disk. Figure 1b shows theoretical iso-contours of yaw angle on a rotor operating at $\mu = 1.0$, with the reverse flow region outlined in red. As a rotor blade completes a single revolution in Figure 1b,

* lsmith1@umd.edu
† arjones@umd.edu

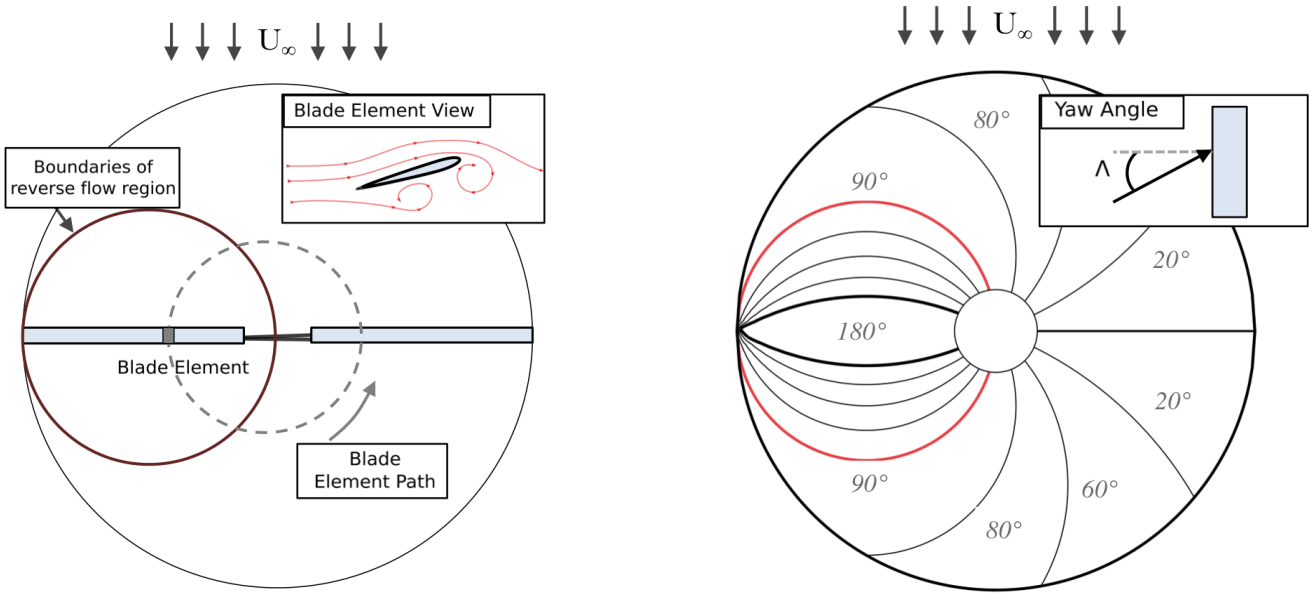

(a) Reverse flow region highlighted on the retreating side.

(b) Iso-contours of yaw angle, adapted from [5].

FIG. 1: Top-down view of the aerodynamic environment encountered by a rotor blade element in forward flight at $\mu = 1.0$. The reverse flow region is highlighted on the retreating side of the rotor in the left subfigure, and iso-contours of yaw angle are sketched atop the rotor disk in the right subfigure.

it encounters a wide range of yaw angles, including a rapid change across $90° < \Lambda < 180°$ in the reverse flow region. The present work simplifies this rapid, time-dependent sweep of yaw angles into just two static yaw angles, $\Lambda = 180°$ and $\Lambda = 150°$. Although it neglects to account for unsteady changes in radial flow, the present work aims to provide a fundamental understanding of how radial flow alters the 2D case of reverse flow dynamic stall, forging a link between previous 2D reverse flow experiments and the unsteady airloads incurred in a full 3D rotor environment.

II. BACKGROUND

In the rotorcraft community, early studies on yawed flow were framed by the "independence principle," or the notion that the airloads produced by a yawed blade are proportional only to the component of the flow parallel to the blade chord. These studies theorized that if the independence principle holds across a rotor blade's operation, the presence of radial flow could be modeled using simple corrections to existing airfoil tables. In an early work on sharp trailing edge airfoils, Purser and Spearman [10] evaluated the independence principle at static angles of attack and static yaw angles in forward flow. The authors found that the independence principle holds at low angles of attack, when the flow is attached, but observed a delay in the onset of lift stall with increasing yaw angle, suggesting the invalidity of the independence principle in separated flow. The delay in lift stall was captured in a radial flow model developed by Gormont [11] for rotorcraft application, but a lack of unsteady experimental data precluded the modeling of flow regimes where separation is significant.

Later work aimed to improve the understanding of yawed flow effects in separated conditions and shifted focus toward the dynamic stall regime. As part of a comprehensive study by the URTC, St Hilaire and Carta [12] monitored the time-dependent force production and surface pressure on an oscillating NACA0012 airfoil in forward flow at two static yaw angles, $\Lambda = 0°$ and $\Lambda = 30°$. The authors found that the presence of yaw delays the onset of lift stall to later times in the pitch cycle and attributed the delay to a significant reduction in the convection speed of the dynamic stall vortex. Lorber [13] validated the delay in lift stall on a finite SC-AA09 wing up to reduced frequencies of 0.15, and Leishman [14], as part of a semi-empirical model of dynamic stall, analyzed yaw effects on trailing edge separation and produced close agreement with St Hilaire and Carta's original data set.

It is important to note that each of the preceding experimental efforts was limited to conventional, sharp-trailing edge airfoils in forward flow. In reverse flow, those same airfoils are dominated by separation about their sharp aerodynamic leading edge, a mechanism that illicits contradictory vortex behavior compared to forward flow dynamic stall. Lim et al. [15], for instance,

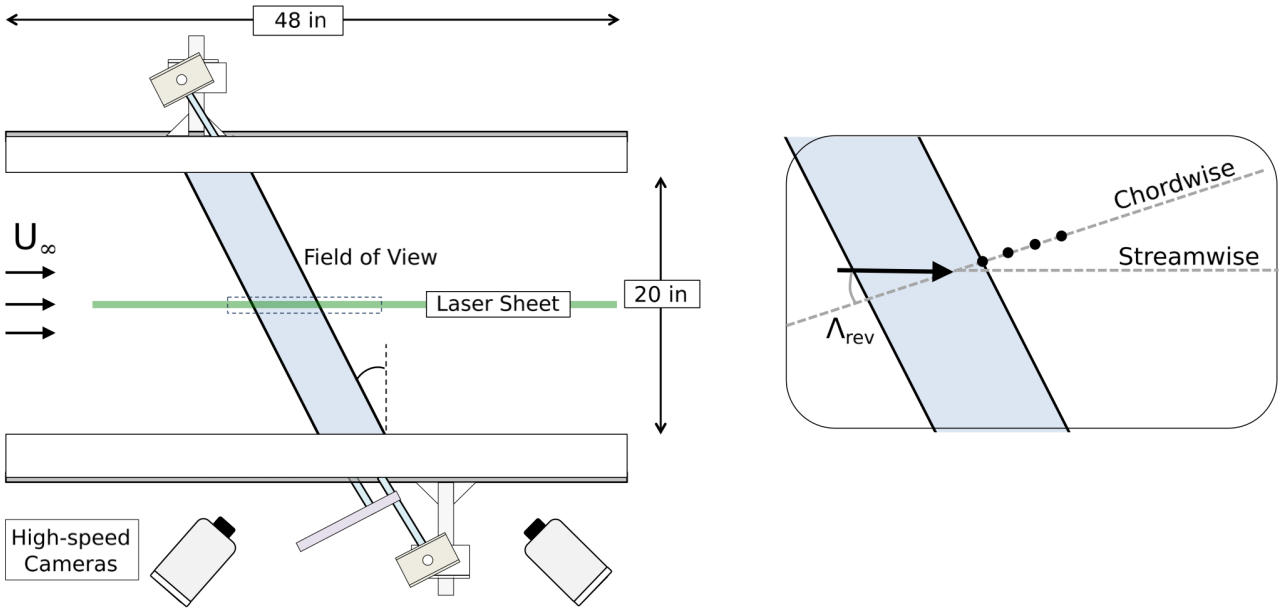

FIG. 2: Experimental setup in the 20 x 28 in low speed wind tunnel at the University of Maryland. The field of view (FOV) is shown at the midspan of the tunnel. Unsteady pressure transducers, represented by black dots in the right-hand subfigure, are installed along the surface of the blade in the chordwise direction.

tracked leading-edge vortex behavior on an impulsively started flat plate at static yaw angles and found very similar vortex positions at $\Lambda = 0°$ and $\Lambda = 25°$. Likewise, Wong et al. [16] noted nearly identical force production on a sinusoidally heaving flat plate at $\Lambda = 0°$ and $\Lambda = 45°$. These results are reported for translating wings at low Reynolds number, but still suggest that the classic effect of yaw on forward flow dynamic stall may not apply to reverse flow, where the mechanism of vortex formation is linked to the airfoil's sharp aerodynamic leading edge.

The present work considers oscillations of a NACA 0012 airfoil at two static yaw angles, $\Lambda = 180°$ and $\Lambda = 150°$. The experiments here seek to relate the presence of spanwise flow to any changes in the stages of reverse flow dynamic stall. Stereoscopic particle image velocimetry allows for characterization of the RFDSV and an assessment of spanwise flow, while unsteady surface pressure transducers link RFDSV behavior to the production of unsteady airloads.

III. METHODOLOGY

For convenience, the present work defines the reverse flow yaw angle, $\Lambda_{rev} = 180 - \Lambda$, relative to the geometric trailing edge of the airfoil. As suggested by Figure 1b, yaw angles in reverse flow range from $\Lambda_{rev} = 0°$ to $\Lambda_{rev} = 90°$. This study compares the flowfields produced by an oscillating NACA0012 airfoil model at two reverse flow yaw angles: $\Lambda_{rev} = 0°$ and $\Lambda_{rev} = 30°$. In the remainder of this work, these conditions will be referred to as the unyawed configuration and the yawed configuration, respectively.

sensor number	x/c position	unyawed	yawed
1	0.2121	x	x
2	0.2798	x	x
3	0.4495	x	x
4	0.5354	x	x
5	0.6061		x
6	0.6768	x	
7	1.0000	x	x

TABLE I: Placement of unsteady pressure sensors along the suction surface of the model, non-dimensionalized by the geometric chord. The sharp edge of the blade corresponds to x/c = 0, while the blunt edge of the blade corresponds to x/c = 1.0

Experiments were performed in a 20 x 28 in low speed, open loop wind tunnel at the University of Maryland. A NACA0012 airfoil model was constructed from acrylic plastic with a geometric chord of 5 in and an aspect ratio of 4. The model was outfitted with a primary 0.375 in stainless steel spar at x/c = 0.75 and a secondary 0.25 in stainless steel spar at x/c = 0.40 . A programmable servo motor, coupled with a four-bar linkage system, allowed for dynamic pitching about the blade's primary spar. Note that this work defines chordwise position relative to the sharp aerodynamic leading edge of the blade.

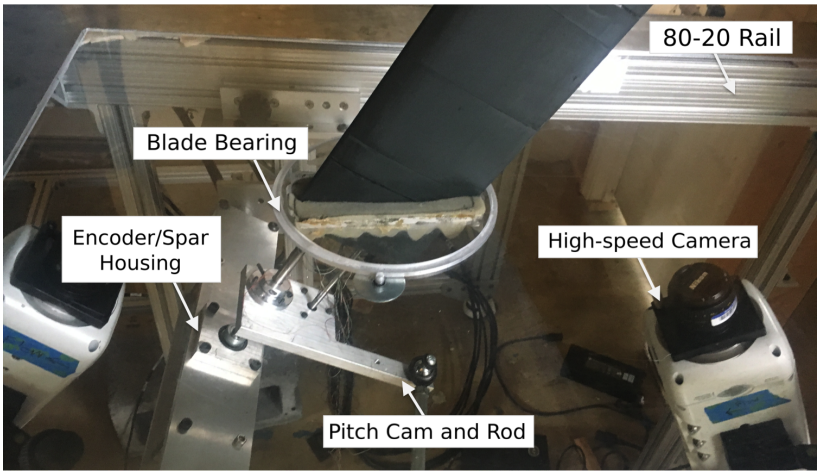

FIG. 3: Photograph of the tunnel mounting apparatus for the blade at $\Lambda_{rev} = 30°$. The blade was passed through the tunnel floor and ceiling by way of a circular bearing and was held in place by a spar housing structure.

The placement of the pitch axis at $x/c = 0.75$ is intended to mirror the orientation of a full-scale rotor blade pitching in the reverse flow region.

Static yaw angles were achieved by fixing the primary spar to a mounting apparatus located atop and below the wind tunnel. Figure 3 shows a photograph of the lower mounting structure and the rail system used to vary yaw angle. The blade was passed through the tunnel floor and ceiling by way of a circular acrylic bearing, and the primary spar was secured to an aluminum housing structure below the test section. A rotary encoder mounted to the primary spar sampled the instantaneous angle of attack. At each static yaw angle, three-component flowfields and surface pressure measurements were collected across a range of reduced frequencies. The following subsections provide an overview of the experimental techniques used to acquire these measurements.

A. Flowfield Measurement

Time-resolved flow fields were collected from stereoscopic particle image velocimetry (PIV) performed at the tunnel midspan. Figure 2 shows the optical setup with the blade installed in the yawed configuration. A high-speed laser, operating at frequencies ranging from 200-500 Hz, illuminated a plane at the midspan of the wind tunnel. Two high-speed 4 Mpx cameras, each placed below the wind tunnel test section, targeted a region near the suction surface of the pitching airfoil. The cameras were tilted to achieve approximately the same field of view, such that the out-of-plane velocity component could be resolved in overlapping regions. Due to difficulties with seeding in open loop wind tunnels, flowfields were collected at a Reynolds number of $Re = 2.5$ x 10^4, much lower than the maximum Reynolds numbers found in a helicopter's reverse flow region. Past experimental campaigns have revealed due to forced flow separation about the blade's sharp edge, reverse flow dynamic stall has a weak sensitivity to changes in Reynolds number [8]. The present work assumes that the flowfield results are generally still applicable to higher Reynolds number flows.

Figure 2 illustrates an important facet of the optical setup: the PIV plane was always parallel to the freestream direction. As a result, the PIV plane in the unyawed configuration is aligned with the airfoil chord, but the PIV plane in the yawed configuration is tilted relative to the airfoil chord. The field of view in turn consists of a different cross-sectional profile depending on the blade's yaw angle. The implications of this difference in cross-section, particularly in relation to the characteristic length scales of the flowfield, are discussed in Section IV.C. For future sections of this work, the term "streamwise" will refer to the orientation of the freestream, while the term"chordwise" will refer to the orientation of the airfoil chord line. This distinction is only relevant when discussing the yawed case, since "streamwise" and "chordwise" refer to the same direction in the unyawed case.

Following data collection, PIV post-processing was completed in several steps. Velocity fields were calculated using DaVis v8.2.3 by LaVision Inc. A multi-pass cross-correlation process, with a minimum window size of 24 x 24 pixels and a 50% overlap, produced a 189 x 110 grid of velocity vectors for each image. The velocity fields were phase-averaged over 10 complete pitching cycles with at least 150 images taken per cycle. Next, the spatial position of a vortex core was determined using the Γ_1 vortex tracking methodology outlined by Graftieaux [19]. The Γ_1 function is a quantitative expression for the extent of circular motion near a certain point in the flowfield. A formula for the Γ_1 function is provided in Equation 2, where S is an area of integration, and θ is the angle be-

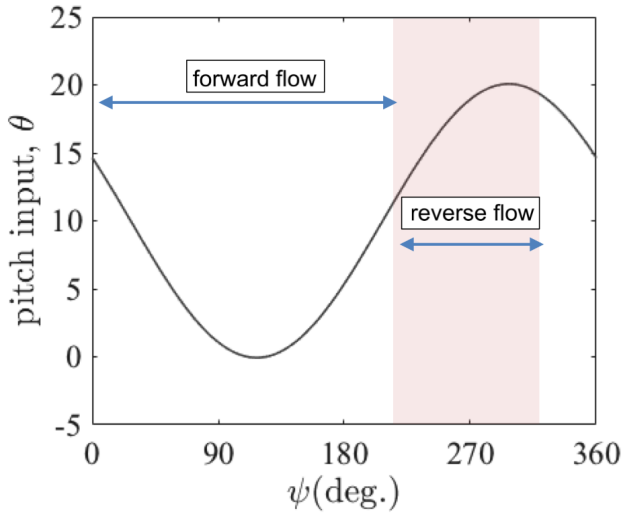

FIG. 4: Pitch input (combined collective and cyclic) for a Mach-scale rotor operating at $\mu = 0.6$, from [17].

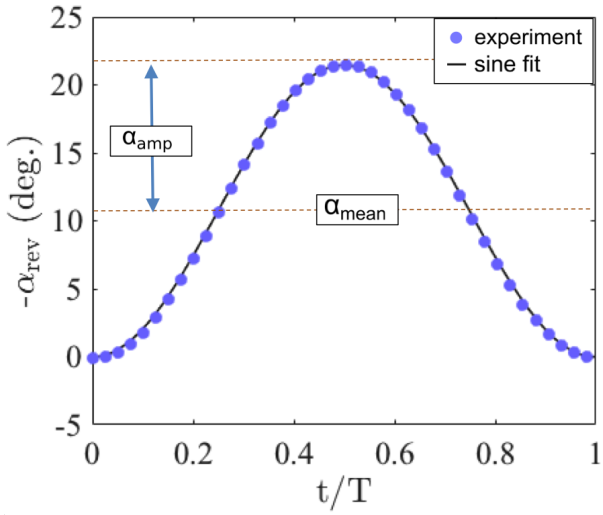

FIG. 5: Pitching kinematics for the baseline reduced frequency in the current work overlaid with an exact sinusoidal fit.

tween the position and velocity vectors at point P.

$$\Gamma_1 = \frac{1}{S}\int_S \sin\theta \mathrm{d}S \tag{2}$$

Vortex cores were quantitatively identified by local peaks in the Γ_1 function and verified with the visual center of rotation in the flowfield. This process generally produced a reliable vortex position for time steps where the RFDSV had convected past the airfoil midchord.

The final step in PIV post processing involved characterization of the RFDSV strength. A 2D control volume was constructed about a portion of the flowfield expected to contain the RFDSV. The lower surface of the volume coincided with the suction surface of the airfoil and extended from $x/c = 0.25$ to $x/c = 1.0$ in the chordwise direction. The upper surface of the control volume coincided with a horizontal line at $z/c = 0.60$ (the upper bound of the field of view) and again extended from $x/c = 0.25$ to $x/c = 1.0$. Within this control volume, an area integral was performed on all negative vorticity, and the resulting circulation was chosen as the measure of RFDSV strength at each time step. Note that the velocity at any point within 0.1 chords of the suction surface was unable to be resolved due to the presence of laser reflections in this region. The ambient temperature and pressure for the majority of PIV runs were approximately 80°F and 30.04 inHg, respectively.

B. Pressure Measurement

Unsteady pressure measurements were collected from Envdevco transducer chips installed along the suction surface of the model. The pressure runs were phase-averaged over 120 pitching cycles at a Reynolds number of 1.0 x 10^5. Table I provides the non-dimensional position of each pressure transducer. In Table I, $x/c = 0$ refers to the sharp aerodynamic leading edge of the model, while $x/c = 1.0$ refers to the blunt aerodynamic trailing edge. The dependence of pressure on span location was addressed by repeating all pressure measurements at 50%, 57.5%, and 65% span. A discussion of spanwise gradients is included Section IV.D. The ambient temperature and pressure for the pressure runs described in Section IV.A were approximately 80°F and 30.10 inHg, while ambient conditions for successive span runs were around 70°F and 30.15 inHg. Note that the sensors were installed in the chordwise direction, meaning pressure measurements are not strictly aligned with the PIV measurements in the yawed configuration.

C. Pitching Kinematics

The kinematics in the current work were specifically chosen to approximate blade elements in the reverse flow region of a high advance ratio rotor, while also forging a connection with past forward flow dynamic stall experiments. Figure 5 shows the variation in reverse flow angle of attack, $\alpha_{\mathrm{rev}} = \alpha - 180°$, with non-dimensional cycle time for a baseline set of pitch kinematics. A sinusoidal fit is overlaid on Figure 5 and shows little variation from the experimental pitch profile. Note that these experiments consist of a single mean pitch angle ($\alpha_{\mathrm{mean}} = 10.75°$), a single pitch amplitude ($\alpha_{\mathrm{amp}} = 10.75°$), but several reduced frequencies.

The sinusoidal pitch motion seen in Figure 5 is intended to mirror the angle of attack experienced by rotor blade elements in reverse flow, but the authors acknowledge that this approach is not without its limitations.

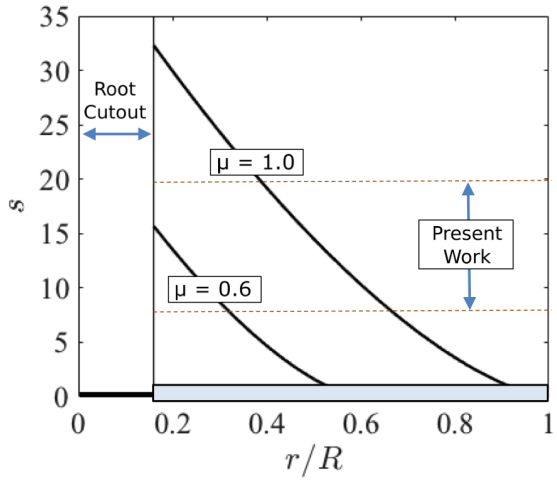

(a) Reduced time distribution.

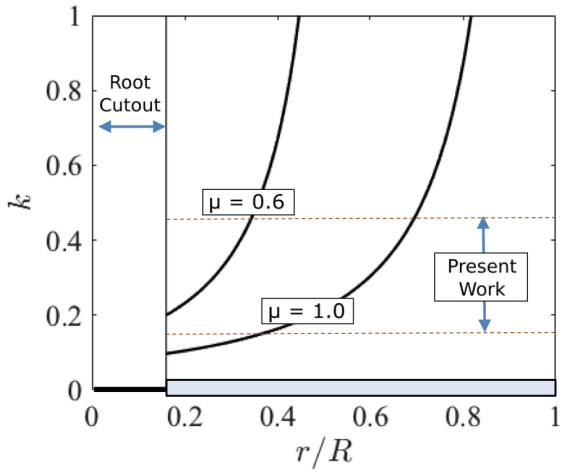

(b) Effective reduced frequency distribution.

FIG. 6: Sample reduced time (left) and effective reduced frequency (right) distributions for a blade element passing through reverse flow. This figure corresponds to a rotor with $R = 40$ in, $c = 3.15$ in, and $\Omega = 900$ RPM, consistent with the experiments in [7, 17, 18]

The local angle of attack on a rotor is determined by the interaction of several aerodynamic features, including the pitch control inputs, the local inflow, and local blade-vortex interactions. Still, outboard blade sections, or sections outside the reverse flow region, generally experience a sinusoidal variation in angle of attack with each blade passage. The majority of conventional dynamic stall experiments have thus been concerned with oscillating airfoils in forward flow. Sinusoidal pitching kinematics are governed by a mean pitch angle, a pitch amplitude, and the reduced frequency, an unsteadiness parameter defined in the equation below:

$$k = \frac{\pi f c}{V_\infty} \tag{3}$$

For outboard blade sections, reduced frequency can be intuitively related to a full-scale rotor environment, as the pitch frequency f corresponds to the blade's 1/rev cyclic pitch control. Inboard sections, however, are complicated by the presence of reverse flow. Figure 4 shows a sample pitch input, or the combination of the rotor's collective and cyclic pitch control, for an inboard section of a Mach-scale rotor [7, 17]. Figure 4 neglects to account for inflow or any interaction with the tip vortex but illustrates an important observation: reverse flow accounts for only a portion of a blade element's revolution. In fact, the pitching kinematics within the reverse flow region have been found to more closely resemble a linear ramp up than a sinusoidal pitch [9]. In turn, pitching in reverse flow is more typically characterized by the reduced time, defined in equation 4, as opposed to the conventional reduced frequency.

$$s = \frac{2}{c}\int_0^t V(t)\,\mathrm{d}t \tag{4}$$

Reduced time is defined as the number of semi-chords traveled by a blade element passing through the reverse flow region. A more general unsteadiness parameter, reduced time can be applied to pitch motions of arbitrary shape and captures the reverse flow region's time-varying freestream. Figure 6a shows the radial distribution of reduced time for a Mach-scale rotor experiment described in reference [7]. This figure was constructed assuming a rotor radius of 33.5 in, a chord of 3.15 in, and an angular velocity of 900 RPM. The present work seeks to produce a data set that can be easily compared to both previous oscillating blade experiments and the parameter space depicted in Figure 6a. As a result, reduced frequencies were chosen such that the "pitch up" portion of the pitching cycle had a similar reduced time to the values seen in Figure 6a. The transformation between this "effective" reduced frequency and the reduced time distribution is given by equation 5.

$$k = \pi/s \tag{5}$$

Figure 6b shows the radial distribution of effective reduced frequency for the same Mach-scale rotor experiments described in reference [7, 17]. The present work focuses on the following four reduced frequencies: $k = 0.160$, 0.217, 0.309, and 0.450. At each reduced frequency, the "pitch up" portion of the pitching cycle is matched to the reduced time for a specific radial location in Figure 6b. For $\mu = 0.6$, the four reduced frequencies correspond to inboard regions of the rotor, where

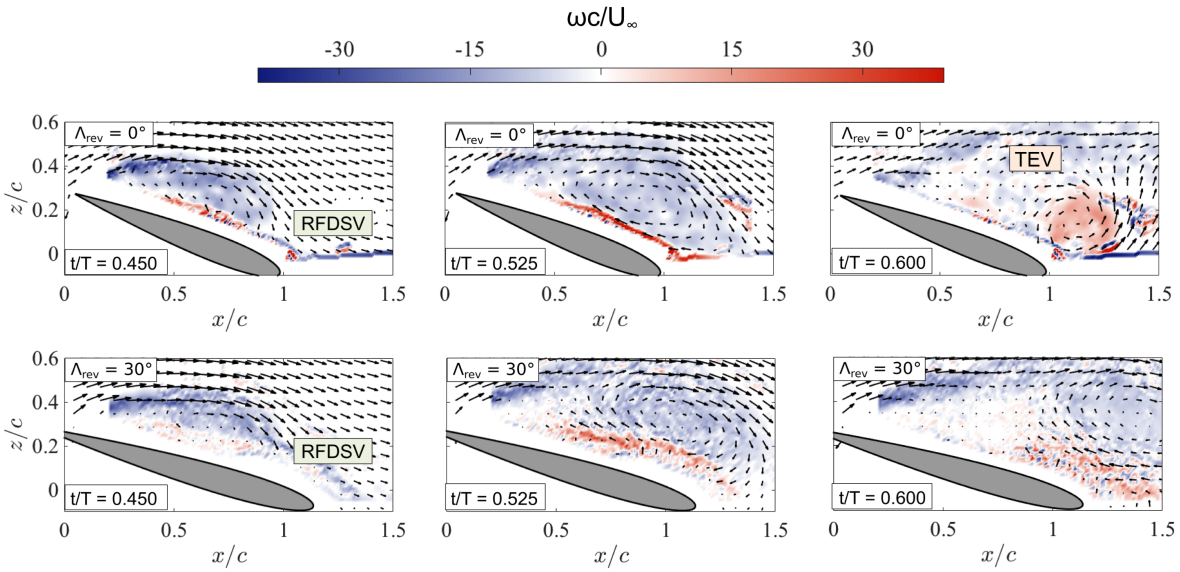

FIG. 7: Identification of relevant flow structures in the unyawed (top) and yawed (bottom) configuration at the baseline reduced frequency, $k = 0.160$. A strong reverse flow dynamic stall vortex (RFDSV) is present at both yaw angles, but a trailing edge vortex (TEV) appears much more coherent in the unyawed case.

dynamic pressure is highest in reverse flow [20]. For $\mu = 1.0$, these reduced frequencies correspond to a large sweep of radial locations from $r/R = 0.4$ to $r/R = 0.7$.

IV. RESULTS AND DISCUSSION

The purpose of this section is to evaluate the effect of yaw on the overall flow morphology of a pitching airfoil in reverse flow. This section will characterize the shedding pattern, or dynamic stall *type*, of the flow in the unyawed and yawed configuration across a range of reduced frequencies. Consistent with the terminology from Lind and Jones [8], dynamic stall *type* is determined based on the number of vortices, both primary and secondary, shed from the blade's leading and trailing edges over the course of a pitch cycle. A type I dynamic stall, for instance, is expected to shed only a single RFDSV over the course of the pitch, while a type III dynamic stall is expected to shed three separate vortices throughout the pitch (a primary RFDSV, a secondary RFDSV, and a trailing-edge vortex). Dynamic stall type has been shown to depend upon mean pitch angle, pitch amplitude, and reduced frequency; the "expected" dynamic stall types in this work are taken from the parameter space mapped by Lind and Jones [8].

The present work will evaluate how the presence of yaw changes the number and strength of vortices shed for a given set of kinematics. Time-resolved flowfield and surface pressure measurements are presented for a single mean pitch angle ($\alpha_{\text{mean}} = 10.75°$); a single mean pitch amplitude ($\alpha_{\text{amp}} = 10.75°$); and two reduced frequencies, $k = 0.160$ and $k = 0.450$. In the unyawed configuration, the "baseline" reduced frequency, $k = 0.160$, is expected to produce a type III dynamic stall, and the "high" reduced frequency, $k = 0.450$, is expected to produce a type I dynamic stall. By varying the dynamic stall type, the following sections consider the effect of yaw on both the reverse flow dynamic stall vortex (RFDSV) and any secondary flow structures that may emerge.

A. Baseline Reduced Frequency, $k = 0.160$

Figure 7 shows phase-averaged flowfields for the unyawed and yawed configuration at the baseline reduced frequency, $k = 0.160$. For each subfigure, non-dimensional chordwise position is plotted on the abscissa, non-dimensional vertical position is plotted on the ordinate, and the velocity vectors are overlaid with contours of non-dimensional vorticity. The freestream velocity travels from left to right such that the sharp geometric trailing edge acts as the aerodynamic leading edge. Recall that $k = 0.160$ corresponds to a type III reverse flow dynamic stall, and the airfoil is expected to shed a primary RFDSV, a trailing edge vortex (TEV), and a secondary dynamic stall vortex (SDSV) at $\Lambda_{\text{rev}} = 0°$.

Consider first the unyawed flowfields shown in the top row of Figure 7. At $t/T = 0.450$, a region of negative vorticity is visible across $0 < x/c < 0.5$, coinciding with flow separation about the sharp aerodynamic leading edge and rollup of the primary RFDSV. By $t/T = 0.525$, the RFDSV has convected to the airfoil's blunt aerodynamic trailing edge, growing substantially as it convects.

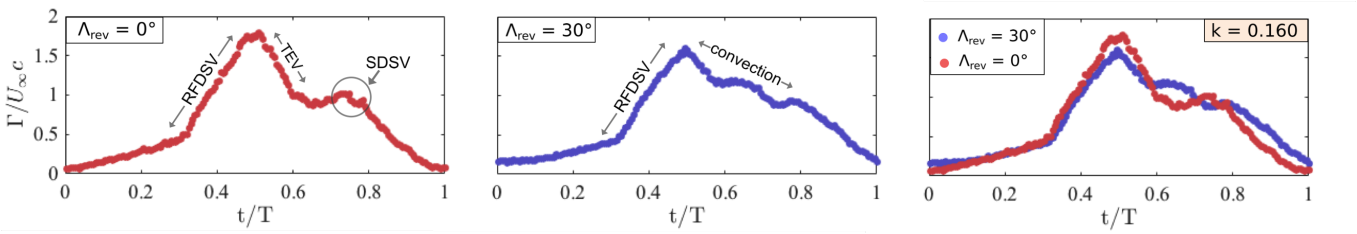

FIG. 8: Evolution of non-dimensional circulation generated by flow structures in the unyawed and yawed configuration. As evidenced by the PIV, the presence of spanwise flow appears to drain vorticity from secondary flow structures and in turn delay the breakup of the RFDSV.

By $t/T = 0.600$, the RFDSV has broken up and is no longer visible. Instead, a strong TEV, incurred by the arrival of the RFDSV at the trailing edge, has appeared on the blade's suction surface and remains coherent for a short time. The TEV results from the generation of positive vorticity and interacts with the RFDSV, an event linked to the breakdown of the RFDSV.

The same time steps are shown for the yawed configuration in the bottom row of Figure 7. Early in the pitch cycle, the yawed flowfields adhere to the basic morphology of reverse flow dynamic stall. Flow separates about the sharp leading edge, rolls up into a RFDSV by $t/T = 0.450$, and convects to the blunt aerodynamic trailing edge by $t/T = 0.525$. The magnitude of negative vorticity, in addition to the relative position of the vortex center, is similar between the yawed and unyawed cases at $t/T = 0.525$. However, differences appear by $t/T = 0.600$. The yawed flowfield shows minimal rotation near the trailing edge, and the amount of positive vorticity is substantially less than in the unyawed case. The RFDSV, rather than being broken apart by interactions with the TEV, is still coherent at $t/T = 0.600$ and convects through the wake undisturbed. Figure 7 suggests that the presence of yaw suppresses the magnitude of secondary flow structures, which in turn allows the primary RFDSV to remain coherent for a greater portion of the pitch cycle.

The impact of yaw on secondary flow structures is further illustrated by the circulation, or total vorticity, generated at $\Lambda_{\text{rev}} = 0°$ and $\Lambda_{\text{rev}} = 30°$. Figure 8 shows the time-evolution of circulation for the unyawed and yawed configuration at the baseline reduced frequency, $k = 0.160$. The unyawed case, seen in the leftmost plot in Figure 8, exhibits a gradual increase in circulation early in the cycle, corresponding to growth of the primary RFDSV, before sharply dropping off over $0.5 < t/T < 0.6$. The sudden decrease in circulation is timed with the convection of the vorticity out of the confines of the circulation box and the breakup of the RFDSV due to interactions with the TEV. Although not visible in Figure 7, a secondary dynamic stall vortex is evidenced by a second circulation peak near $t/T = 0.750$ in Figure 8 as the blade completes its pitch down. These three flow structures, the primary RFDSV, the TEV, and a SDSV, align with the predicted flow features of a type III reverse flow dynamic stall [8].

The yawed case, illustrated by the middle plot in Figure 8, exhibits a slightly different time evolution of circulation. At $\Lambda_{\text{rev}} = 30°$, circulation increases over the pitch-up portion of the cycle, again corresponding to formation of the primary RFDSV, but does not suddenly decrease immediately following the peak. Instead, circulation slowly drops over $0.5 < t/T < 0.8$, with the yawed case maintaining slightly higher values of circulation compared to the unyawed case over the same interval. The absence of a sharp decline is directly related to the absence of a strong TEV in the yawed case. Without the influence of a TEV, the RFDSV maintains its coherence and simply convects out of the circulation box, resulting in a more gradual drop in circulation. A secondary circulation peak, which appeared near $t/T = 0.750$ when $\Lambda_{\text{rev}} = 0°$, is significantly suppressed at $\Lambda_{\text{rev}} = 30°$. The presence of yaw at $k = 0.160$ appears to produce a flow field more closely aligned with the features of a type I dynamic stall, where the pitch cycle is dominated by just a single RFDSV, instead of a type III dynamic stall, which was predicted for the unyawed case.

The next step of this analysis will relate the stages of reverse flow dynamic stall, including their dependence on yaw angle, to the airloads generated at $\Lambda_{\text{rev}} = 0°$ and $\Lambda_{\text{rev}} = 30°$. Figure 9 shows the time evolution of surface pressure in the unyawed (left) and yawed (right) configurations at the baseline reduced frequency, $k = 0.160$. In this figure, non-dimensional cycle time is plotted on the abscissa, and pressure coefficient, adjusted here to visually scale the sensor readings, is plotted on the ordinate. A grey shaded region surrounds each sensor reading and represents two standard deviations from the solid phase-averaged line. A color-coded triangle, included for stations where $x/c > 0.5$, denotes the time at which the RFDSV, as determined from PIV, passes over the chordwise location of each pressure sensor.

As an introduction to the changes in surface pressure experienced during reverse flow dynamic stall, consider the readings from the sensor at $x/c = 0.4495$, highlighted in the leftmost plot of Figure 10. Early in the pitch cycle, this sensor's readings remain fairly constant, with little deviation from the value of freestream dynamic pressure. Near $t/T = 0.35$, the pressure magnitude begins to change abruptly, reaching its minimum value near

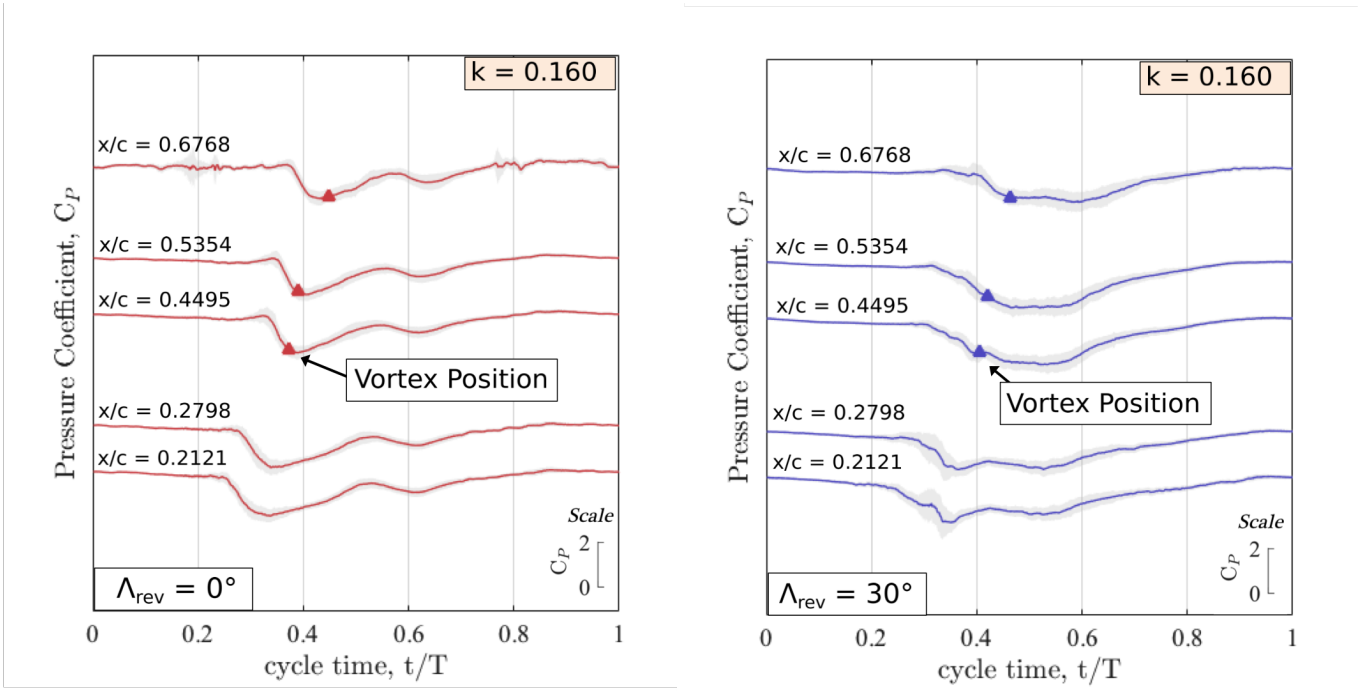

FIG. 9: Appearance of low pressure impulse in the unyawed configuration (left) and yawed configuration (right) at the baseline reduced frequency, $k = 0.160$.

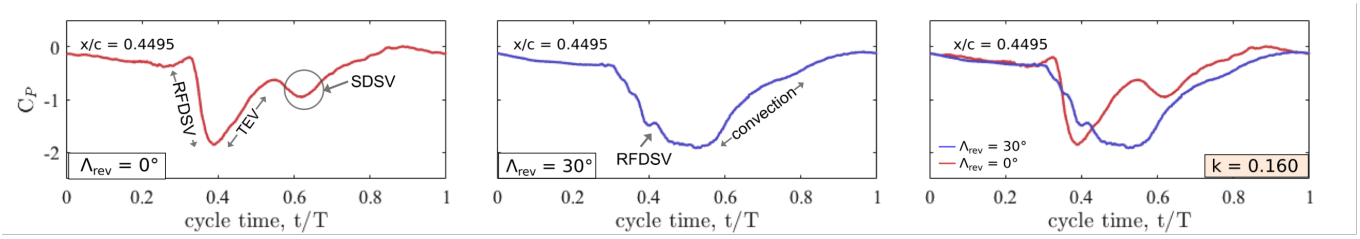

FIG. 10: Comparison of pressure impulse shape in the unyawed and yawed configuration at $k = 0.160$. The difference in pressure impulse shape highlights the importance of the trailing edge vortex (TEV) in breaking down the reverse flow dynamic stall vortex (RFDSV).

$t/T = 0.4$. The minimum pressure is sustained briefly before the pressure quickly begins increasing back toward the freestream. A second local minimum, of much lower magnitude than the previous peak, is exhibited at $t/T = 0.6$. The timing of each pressure peak aligns with the passage of a vortex over $x/c = 0.45$. The first peak aligns with the formation of the primary RFDSV, denoted by the red triangle in Figure 9, while the second peaks aligns with the passage of the SDSV. Looking at downstream sensors in Figure 9, the two peaks still occur but at progressively later points in the pitch cycle, signifying the convection of these two vortices along the airfoil chord.

The yawed pressure history for $x/c = 0.45$ is shown in the middle plot of Figure 10. The pressure at $\Lambda_{\text{rev}} = 30°$ again exhibits little variation early in the cycle before beginning a sudden decrease near $t/T = 0.35$. A minimum pressure is initially reached near $t/T = 0.4$ but is maintained for a significantly longer portion of the cycle compared to $\Lambda_{\text{rev}} = 0°$. The second minimum in pressure, which occurred near $t/T = 0.6$ at $\Lambda_{\text{rev}} = 0°$, is completely absent from the pressure history at $\Lambda_{\text{rev}} = 30°$. Consistent with the flowfield measurements, the pressure history in the yawed configuration appears to be characterized by only a primary RFDSV and absent secondary flow structures. The absence of a strong TEV delays the breakup of the primary RFDSV, which extends the amount of time it exerts a low pressure at $x/c = 0.45$, and the absence of a strong SDSV precludes a second local minimum in pressure. These trends for the yawed case, wherein the pressure history is dominated by a single, more sustained drop in pressure, are evident in the remaining sensors on the right-hand side of Figure 9.

This analysis has thus revealed an important feature of yawed airfoils in reverse flow. The presence of yaw at $k = 0.160$ appears to impede the development of sec-

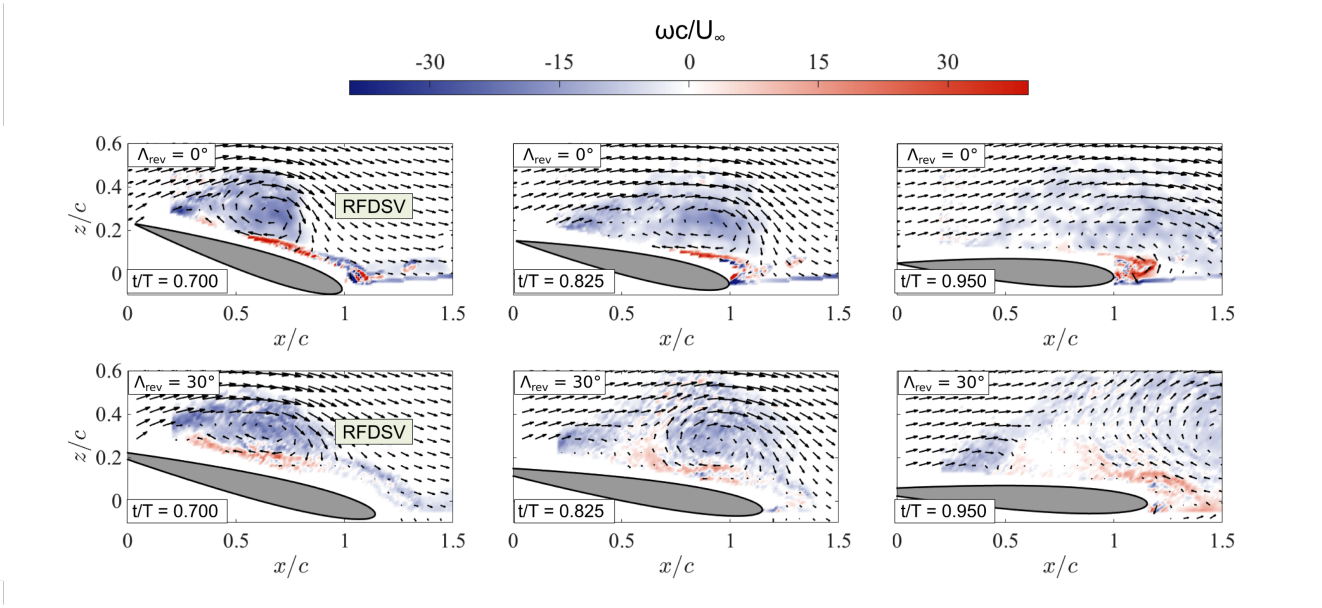

FIG. 11: Identification of relevant flow structures in the unyawed (top) and yawed (bottom) configuration at the "high" reduced frequency, $k = 0.450$. Here, the behavior of the reverse flow dynamic stall vortex (RFDSV) is remarkably similar when the blade is either yawed or unyawed, as the trailing edge vortex is absent from both cases.

ondary flow structures, and the resulting flow field is dominated only by a primary RFDSV that convects along the airfoil chord. The next section will perform the same flowfield and pressure analysis on a pitching airfoil at higher reduced frequency, where the flow is not expected to develop any secondary flow structures. If the primary effect of yaw is indeed to suppress the development of the TEV and SDSV, then the following high reduced frequency case, where these features do not develop, is expected to yield very similar flowfields and surface pressure measurements at both $\Lambda_{\text{rev}} = 0°$ and $\Lambda_{\text{rev}} = 30°$.

B. High Reduced Frequency, $k = 0.450$

Figure 11 shows phase-averaged flowfields for the unyawed and yawed configuration at the high reduced frequency of $k = 0.450$. The flowfield at $\Lambda_{\text{rev}} = 0°$, plotted in the top row of Figure 11, closely adheres to the predicted features of a type I dynamic stall. A primary RFDSV forms due to separation about the sharp leading edge and convects along the chord over $0.7 < t/T < 0.825$. The RFDSV reaches the trailing edge of the unyawed airfoil by $t/T = 0.90$ but does not incur the rollup of a TEV, meaning the RFDSV stays coherent as it convects into the wake. The flowfield at $\Lambda_{\text{rev}} = 30°$, plotted in the bottom row of Figure 11, also exhibits the same basic features expected of a type I dynamic stall. An RFDSV forms, grows, and convects but does not result in the formation of a TEV before the end of the pitch cycle.

With such similar flowfields, the unyawed and yawed configuration are expected to yield very similar airfloads, as neither resulted in any visible secondary flow structures. Figure 12 shows the time-evolution of surface pressure (left) and the time-evolution of circulation (right) for $\Lambda_{\text{rev}} = 0°$ and $\Lambda_{\text{rev}} = 30°$ in the high reduced frequency case, $k = 0.450$. Note that the pressure measurements in Figure 12 were collected at a slightly lower Reynolds number ($Re = 5$ x 10^4) compared to previous pressure measurements ($Re = 1$ x 10^5), resulting in a lower signal to noise ratio. Figure 12 reveals very similar surface pressure and circulation histories between the two configurations. In the pressure time histories, both the unyawed and yawed conditions begin at a nominal freestream pressure before dropping to single minimum, the duration of which is consistent at $\Lambda_{\text{rev}} = 0°$ and $\Lambda_{\text{rev}} = 30°$. In the circulation histories, each configuration is dominated by a single rise and drop in circulation, attributed to the formation and growth of a primary RFDSV, and reaches the same maximum near $t/T = 0.75$. The differences in circulation behavior, which were readily apparent at $k = 0.160$, seem to disappear when the reduced frequency is increased to $k = 0.450$.

Comparing the results of the baseline and high reduced frequencies, the effect of yaw quickly becomes apparent. At $k = 0.160$, the unyawed flowfield showed a strong RFDSV, TEV, and SDSV, while the yawed flowfield showed only a strong RFDSV and weak secondary structures. In turn, the behavior of the surface pressure and circulation production varied significantly between $\Lambda_{\text{rev}} = 0°$ and $\Lambda_{\text{rev}} = 30°$. At $k = 0.450$, neither the unyawed nor the yawed configuration resulted in strong secondary flow features. In this case, the surface pressure and circulation were remarkably similar between the two configurations. The preceding analysis seems to confirm

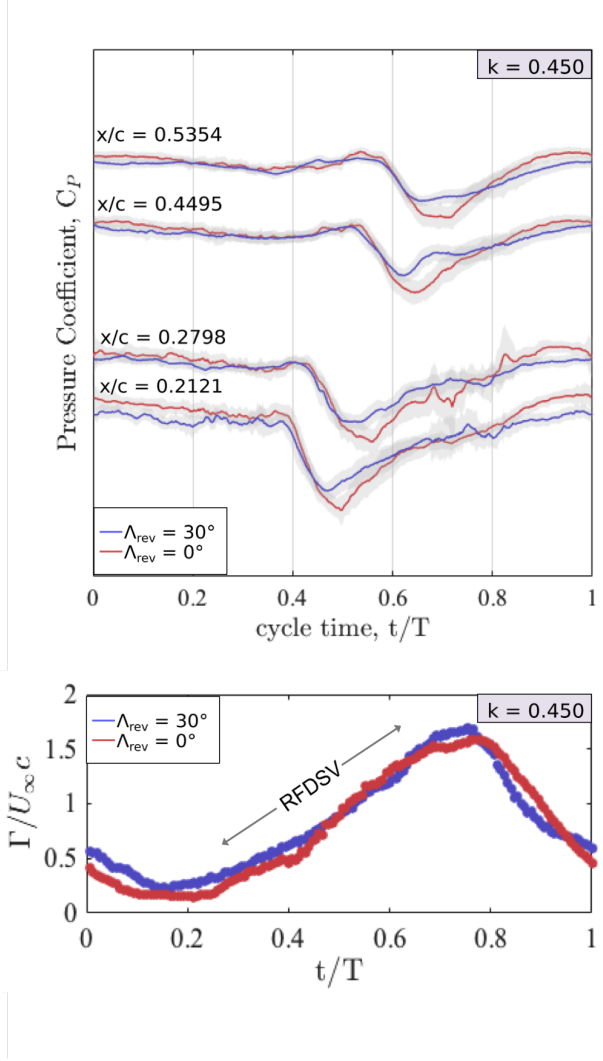

FIG. 12: Comparison of surface pressure (top) and circulation (bottom) evolution for the unyawed and yawed case at $k = 0.450$. Since secondary flow structures are absent from both configurations, the time histories of pressure and circulation are very similar between $\Lambda_{rev} = 0°$ and $\Lambda_{rev} = 30°$.

the notion that the presence of yaw primary affects the flowfield by hindering the development of secondary flow structures.

The present work considers two explanations for this phenomenon. First, the weakening of the TEV may be attributed to a difficulty in properly scaling the kinematics of the yawed blade. Due to the unconventional orientation of the blade at $\Lambda_{rev} = 30°$, the appropriate length and velocity scales of the flow in this configuration are not immediately obvious. Reduced frequency, for instance, was defined according to the geometric chord (5 in) and streamwise velocity (V_∞), but different scalings may very well result in a different shedding pattern. Second, the suppression of all secondary flow structures may be due to transport of vorticity along the blade span. Previous experimental work on yawed flows, particularly recent investigations on rotating wings [21, 22], have theorized that spanwise flow has a "draining" effect on vorticity production. This "draining" effect requires the presence of spanwise gradients in the flowfield, which are presumed to be small in these experiments, but the effect may still be enough for secondary flow structures to be impacted , as they produce less vorticity overall. The remainder of this work will investigate these two ideas as potential explanations for the suppression of secondary flow features.

C. Scaling Parameters

The kinematics studied in this work were defined in Section 3.3 by a mean pitch angle, a pitch amplitude, and a reduced pitch frequency. At $\Lambda_{rev} = 0°$, these parameters are unambiguous. The blade chord is aligned with the oncoming freestream, and the blade pitch axis is perpendicular to the freestream. At $\Lambda_{rev} = 30°$, defining the kinematics becomes less intuitive. The blade chord is now tilted, changing the "effective" blade cross-section in the streamwise direction, and the blade pitch axis is no longer parallel to the oncoming freestream. It is thus less clear whether to define the kinematics relative to the blade chordwise direction, or relative to the freestream flow. This subsection will consider various ways of scaling the blade kinematics and how these alternate scalings impact the vortex shedding pattern.

Consider first the reduced frequency, defined initially in Equation 3. For the results presented in previous sections, the reduced frequency was scaled according to the geometric chord and the freestream velocity (i.e., the streamwise velocity in the yawed case). This definition was chosen such that vortices in the PIV frame saw approximately the same streamwise convection speed for both $\Lambda_{rev} = 0°$ and $\Lambda_{rev} = 30°$. Figure 13, which plots the chordwise position of the vortex center over time, shows this assumption to be largely true, as the two configurations have similar convection behavior across $0.160 < k < 0.450$. It must be kept in mind, however, that the blade at $\Lambda_{rev} = 30°$ has a longer effective chord than in the PIV frame $\Lambda_{rev} = 0°$. In Figure 13, the blade trailing edge for $\Lambda_{rev} = 30°$ corresponds to roughly $x/c \approx 1.15$, meaning the RFDSV reaches the trailing edge at a later point in the pitch cycle for the yawed case compared to the unyawed case. It is thus unclear whether the difference in shedding pattern reported in Section IV.A is due simply to the longer effective chord at $\Lambda_{rev} = 30°$, or whether the presence of yaw adds new physics to the flow.

An attempt to account for the difference in "effective" chord between the two configurations is provided in Figure 14. Here, an adjusted reduced frequency k^* is defined in Equation 6 such that the effective chord is used as the

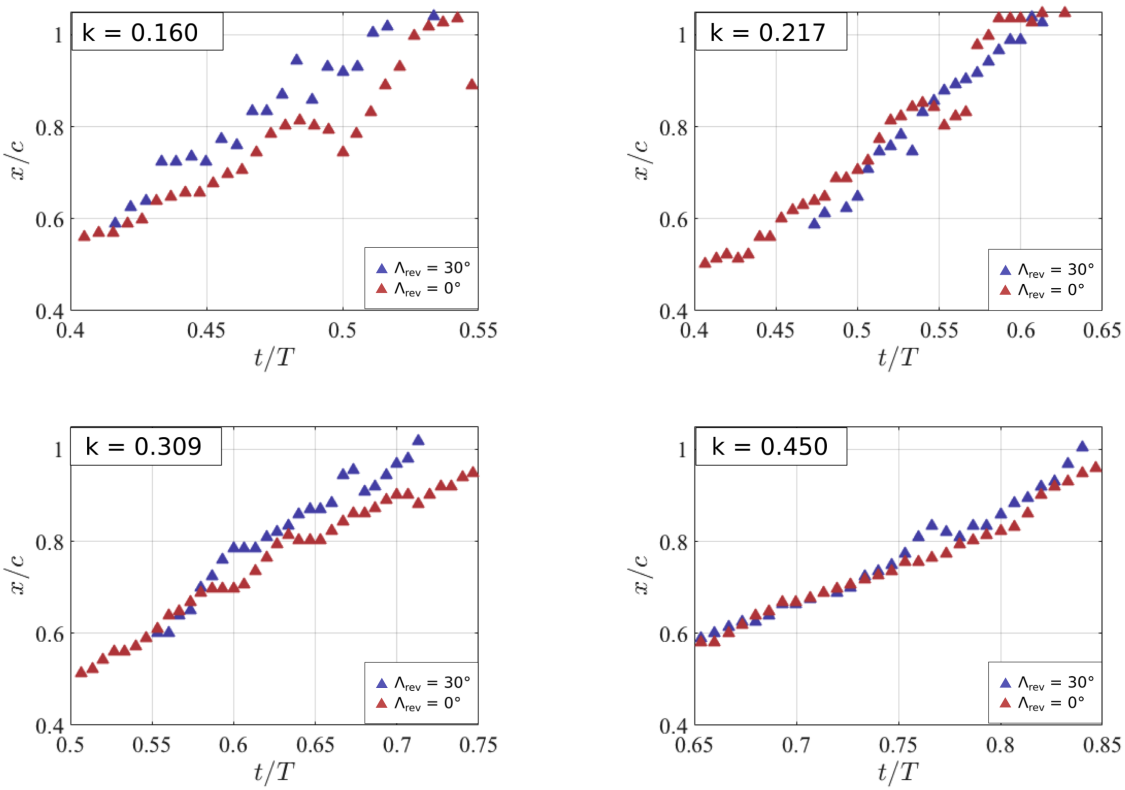

FIG. 13: Vortex center as calculated from the Γ_1 function. The results are non-dimensionalized by the *geometric* chord of 5 in for both cases. Note the similarity between the yawed and unyawed cases.

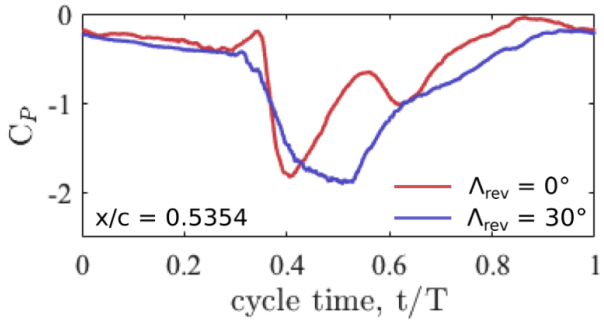

FIG. 14: Comparison of pressure impulse shape in the unyawed and yawed configuration when the adjusted reduced frequency is matched ($k^* = 0.160$). Even when the RFDSV is expected to reach the trailing edge at the same time, the difference in pressure impulse shape persists.

characteristic length scale of the flowfield.

$$k^* = \frac{\pi f c}{2V_\infty \cos(\Lambda_{rev})} \tag{6}$$

Figure 14 plots the pressure coefficient for $\Lambda_{\text{rev}} = 0°$ and $\Lambda_{\text{rev}} = 30°$ at a matched adjusted reduced frequency of $k^* = 0.160$. Note that a matched k^* was achieved by increasing the freestream velocity in the yawed case, effectively matching the chordwise velocity between the two configurations. Thus, the RFDSV is expected to reach the airfoil's trailing edge at the same point in the cycle for both $\Lambda_{\text{rev}} = 0°$ and $\Lambda_{\text{rev}} = 30°$. Despite the matched chordwise velocity, Figure 14 shows that the two configurations still produce very different pressure histories over time. The unyawed configuration is still marked by two sharp dips in pressure, while the yawed configuration is still dominated by a single, more sustained negative peak. Figure 14 suggests that the difference in shedding pattern between $\Lambda_{\text{rev}} = 0°$ and $\Lambda_{\text{rev}} = 30°$ cannot be attributed to a difference in the effective chord length in the yawed configuration.

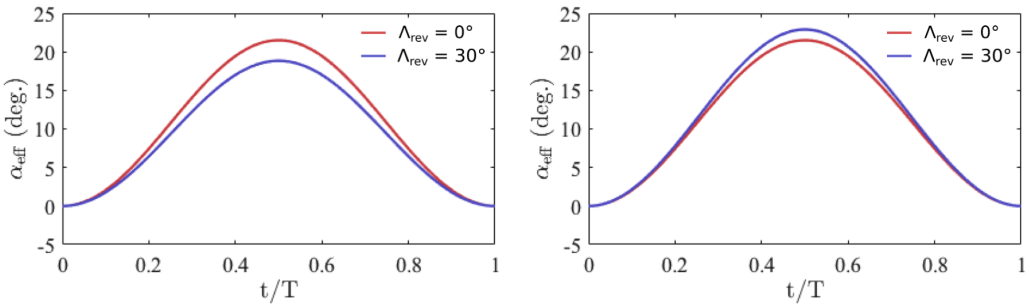

FIG. 15: The "effective," or streamwise, pitch angle for the unyawed and yawed configuration at the baseline kinematics (left, $\alpha_{mean} = 10.75°$, $\alpha_{amp} = 10.75°$) and the corrected kinematics (right, $\alpha_{mean} = 13°$, $\alpha_{amp} = 13°$). Note that the effective pitch angle nearly matches throughout the cycle for the corrected case

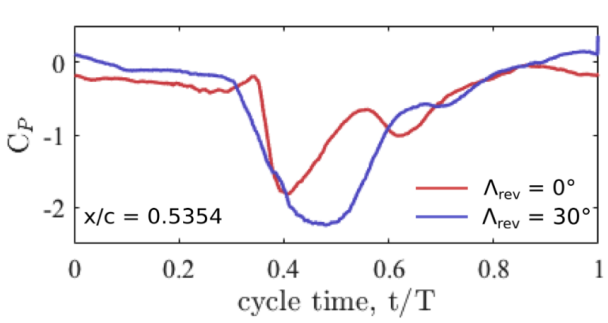

FIG. 16: Comparison of pressure impulse shape in the unyawed and yawed configuration when the effective pitch angle is matched at constant reduced frequency, $k = 0.160$.

Next, consider the effect of yaw on the blade's mean pitch angle and pitch amplitude. When the blade is yawed, its pitch axis remains parallel to the blade span. This means that the "effective" pitch amplitude, or the pitch amplitude relative to the streamwise flow direction, is different at $\Lambda_{rev} = 30°$ compared to $\Lambda_{rev} = 0°$. Geometric analysis leads to the following transformation between the "effective" blade pitch angle (α_{eff}) and the nominal pitch angle (α, defined relative to the chordwise direction).

$$\tan(\alpha_{eff}) = \tan\alpha\big(\cos\Lambda_{rev}\big) \tag{7}$$

The effective pitch angle for the baseline kinematics ($\alpha_{amp} = 10.75°$, $\alpha_{mean} = 10.75°$) is plotted against non-dimensional cycle time in the lefthand side of Figure 15. Note that the maximum effective pitch angle is somewhat lower in the yawed case compared to the unyawed case. Past experimental campaigns have shown that dynamic stall type is sensitive to changes in mean pitch angle and pitch amplitude, meaning the difference seen in the lefthand side of Figure 15 is a potential contributor to the change in vortex shedding pattern between $\Lambda_{rev} = 0°$ and $\Lambda_{rev} = 30°$. An effort to correct for the difference in effective pitch angle was undertaken by repeating the experiments at an effective mean pitch angle of $\alpha_{mean} = 13°$ and a pitch amplitude of $\alpha_{amp} = 13°$. Illustrated in the righthand side of Figure 15, this increase leads to an effective pitch angle that closely matches between the $\Lambda_{rev} = 0°$ and $\Lambda_{rev} = 30°$ cases throughout the pitch cycle. Figure 16 shows a representative pressure reading when the effective pitch angle is matched for the unyawed and yawed configuration. The pressure time history at $\Lambda_{rev} = 30°$ is still characterized by a single, sustained peak in negative pressure, again suggesting that secondary flow features are suppressed despite the corrected pitch angle.

As a final comment on potential scaling laws for the yawed blade, Figure 17 compares a representative pressure reading for $\Lambda_{rev} = 0°$ and $\Lambda_{rev} = 30°$ at a matched adjusted reduced frequency, $k^* = 0.160$, and a matched effective pitch angle (i.e., $\alpha_{mean} = 13°$ and $\alpha_{amp} = 13°$). This figure represents a case corrected for both the difference in effective chord length and effective pitch ampltude. Qualitatively, the two configurations seem similar in Figure 17. The magnitude of the negative pressure peak is comparable between the two cases, and the duration of the pressure peak at $\Lambda_{rev} = 30°$ is reduced compared to previous iterations. However, the yawed case still shows little evidence of the secondary flow features seen in the unyawed case. The yawed shedding pattern, wherein the yawed blade sheds only a single primary RFDSV, appears to be insensitive to alternate scalings of the pitch kinematics and freestream velocity.

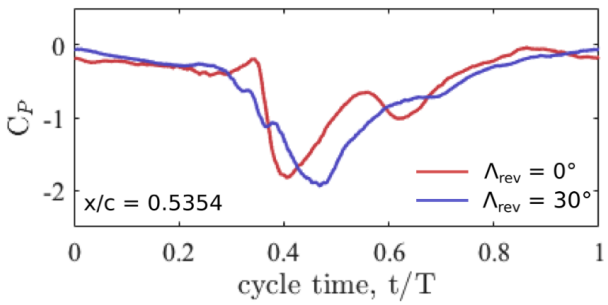

FIG. 17: Comparison of pressure impulse shape in the unyawed and yawed configuration when the effective pitch angle is matched at constant adjusted reduced frequency, $k^* = 0.160$.

D. Spanwise Transport of Vorticity

The preceding sections characterized reverse flow dynamic stall in the unyawed and yawed configuration but were limited to two-component flowfield measurements at the tunnel midspan. The purpose of this section is to quantify the magnitude of the third velocity component, or spanwise flow, and investigate the possibility of a net transport of vorticity along the blade span. Note that the current PIV measurements do not permit the direct quantification of spanwise flow gradients. Instead of directly quantifying spanwise transport through flow gradients, this section seeks to prove that some degree of spanwise transport exists on the yawed blade, and that this transport is likely greater at $\Lambda_{\text{rev}} = 30°$ compared to $\Lambda_{\text{rev}} = 0°$. In light of the small effect of kinematic variations on the yawed blade shedding pattern (see Section IV.C), the current work posits that spanwise transport, if it is indeed shown to exist, is the most likely explanation for the suppression of secondary flow features at $\Lambda_{\text{rev}} = 30°$.

To begin, consider the blade in its yawed orientation, as depicted in the lefthand side of Figure 18. A coordinate system (x, y, z) can be defined such that that the x-coordinate aligns with the chordwise direction, and the z-coordinate aligns with the spanwise direction. The transport of spanwise vorticity, or ω_z, for an arbitrary planar volume in this coordinate system is governed by Equation 8.

$$\frac{\partial \omega_z}{dt} + \frac{\partial(\omega_z u_x)}{\partial x} + \frac{\partial(\omega_z u_y)}{\partial y} = \frac{\partial(\omega_x u_z)}{\partial x} + \frac{\partial(\omega_y u_z)}{\partial y} + \nu \frac{\partial^2 \omega_z}{\partial x_j^2} \tag{8}$$

Equation 8 represents the vorticity formulation of the Navier Stokes equation for an incompressible, three-dimensional flow. A formal derivation of Equation 8 can be found in Medina et al. [22]. Of particular interest to the present work are the first two terms on the righthand side of Equation 8, collectively representing the change in spanwise vorticity due to the tilting of the local vorticity vector. A more useful form of these "3D effects" terms can be found by noting that the 3D vorticity vector is divergence free. Thus:

$$\frac{\partial(\omega_x u_z)}{\partial x} + \frac{\partial(\omega_y u_z)}{\partial y} = -u_z \frac{\partial \omega_z}{\partial z} + \omega_x \frac{\partial u_z}{\partial x} + \omega_y \frac{\partial u_z}{\partial y} \tag{9}$$

Equation 9 decomposes the 3D physics of the flowfield into terms associated with the spanwise convection of vorticity (first term on the righthand side) and the spanwise tilting of in-plane vorticity components (second and third terms on the righthand side). If we focus only on the spanwise convection term, vorticity transport can be shown to exist at $\Lambda_{\text{rev}} = 30°$ if there is both a spanwise flow, u_z, and a spanwise gradient of vorticity, $\frac{\partial \omega_z}{\partial z}$. Each of these components will addressed in the figures that follow.

Figure 19 shows contours of spanwise flow for the yawed configuration (bottom) and, for comparison, the unyawed configuration (top) at $k = 0.217$. Velocity vectors, shown in black, are overlaid on Figure 19 to visualize the approximate location of the vortex center and flow separation. In Figure 19, a red contour indicates flow toward the tunnel floor, the expected direction for the yawed case, while a blue contour indicates flow toward the tunnel ceiling.

The top row of Figure 19 shows that the unyawed case, despite having its chord aligned with the tunnel freestream, generates a small amount of flow along the blade span. This spanwise flow is thought to be a result of either leaks in the wind tunnel test section, a consequence of the blade passing through the tunnel ceiling and floor, or three-dimensional effects associated with tunnel end-wall condition [23]. On the whole, however, the magnitude of spanwise flow in the unyawed case is small compared to the yawed case, illustrated in the bottom row of Figure 19. Here, the entire flowfield is covered with a large amount of spanwise flow. The magnitude of this flow fluctuates in regions of flow separation, but its value still remains a quarter of the freestream at its weakest. Figure 19 suggests that, as expected, the area surrounding the yawed blade is subject to substantially more spanwise flow at $\Lambda_{\text{rev}} = 30°$ compared to $\Lambda_{\text{rev}} = 0°$.

Next, consider the pressure time histories provide in the righthand side of Figure 18. This plot represents surface pressure measurements for the yawed blade at

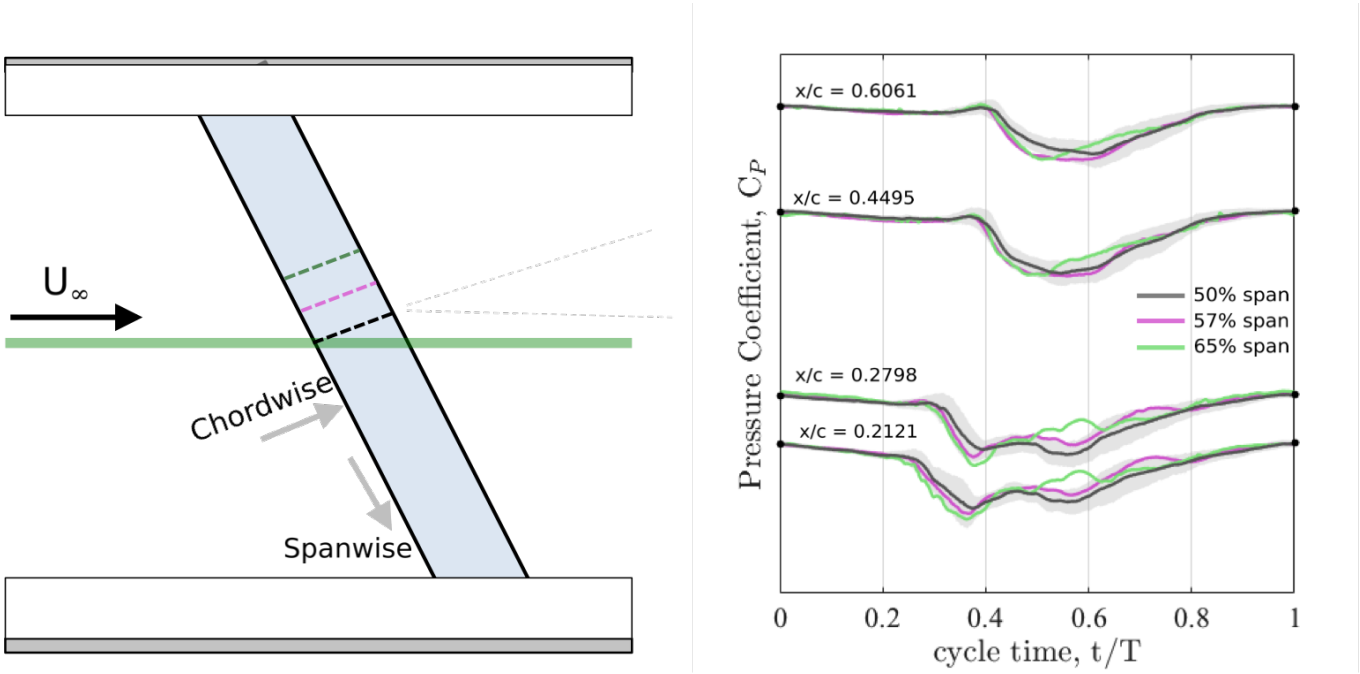

FIG. 18: Definition of expected chordwise and spanwise flow directions, with an illustration of the impact of spanwise variation on surface pressure.

$k = 0.217$ repeated over multiple spanwise locations to assess possible gradients along the blade span. For each of the four sensors shown in Figure 18, the pressure signals reveal a small but certainly non-zero variation in surface pressure along the span, particularly during the "spike" portion of the pressure history. Section IV.A illustrated that this spike in pressure is inherently related to the convection of the RFDSV. The spanwise gradient in pressure, then, seems to suggest non-uniformity in the formation and convection of the RFDSV at different span locations. Stated a different way, the righthand side of Figure 18 provides evidence for a spanwise gradient in the local vorticity, $\frac{\partial \omega_z}{\partial z}$, near the location of the RFDSV.

The current work argues that Figures 18 and 19 provide evidence that the magnitude of spanwise transport is greater in the yawed case compared to the unyawed case. To illustrate this, consider that the spanwise variations in pressure seen in Figure 18 are not inherent to the flow. They must instead be attributed to irregularities in the blade's surface finish, leaks in the tunnel at the floor or ceiling, or the tunnel wall condition; that is, these non-uniformities are present in both unyawed and yawed configutations. At $\Lambda_{\text{rev}} = 0°$, spanwise non-uniformities do not appear to be particularly significant, as the spanwise convection term $(u_z \frac{\partial \omega_z}{\partial z})$ remains small by virtue of the small spanwise flow magnitude. At $\Lambda_{\text{rev}} = 30°$, the spanwise convection term is multiplied by a significant magnitude of spanwise flow, meaning the spanwise convection term risks becoming non-negligible. The results presented here suggest that this magnification of the spanwise convection term is enough to a cause a somewhat significant transport of vorticity in certain regions of the flowfield, ultimately manifesting in the suppression of weaker, secondary flow structures.

V. CONCLUSIONS

In an effort to model the large torsional loads incurred by the rotors at high advance ratio, experimental work has sought to develop a physical understanding of dynamic stall in reverse flow. The present work addresses the influence of yaw on the primary and secondary features of reverse flow dynamic stall. A subscale model rotor blade was held at two static yaw angles in reverse flow, $\Lambda_{\text{rev}} = 0°$ (unyawed) and $\Lambda_{\text{rev}} = 30°$ (yawed), and dynamically pitched about its geometric quarter-chord. Dynamic pitching was completed for a single mean pitch angle, a single pitch amplitude, and multiple reduced frequencies from $k = 0.160$ to $k = 0.450$. Three-component velocity fields were obtained from stereoscopic particle image velocimetry, and surface pressure time histories were obtained using discrete unsteady pressure transducers installed at positions along the suction surface of the model. Analysis of these data led to the following conclusions:

- The presence of yaw appears to suppress the magnitude of secondary flow structures. At $k = 0.160$, the flowfield of the unyawed blade features a distinct primary reverse flow dynamic stall vortex (RFDSV), trailing edge vortex (TEV), and secondary dynamic stall vortex (SDSV). At the same

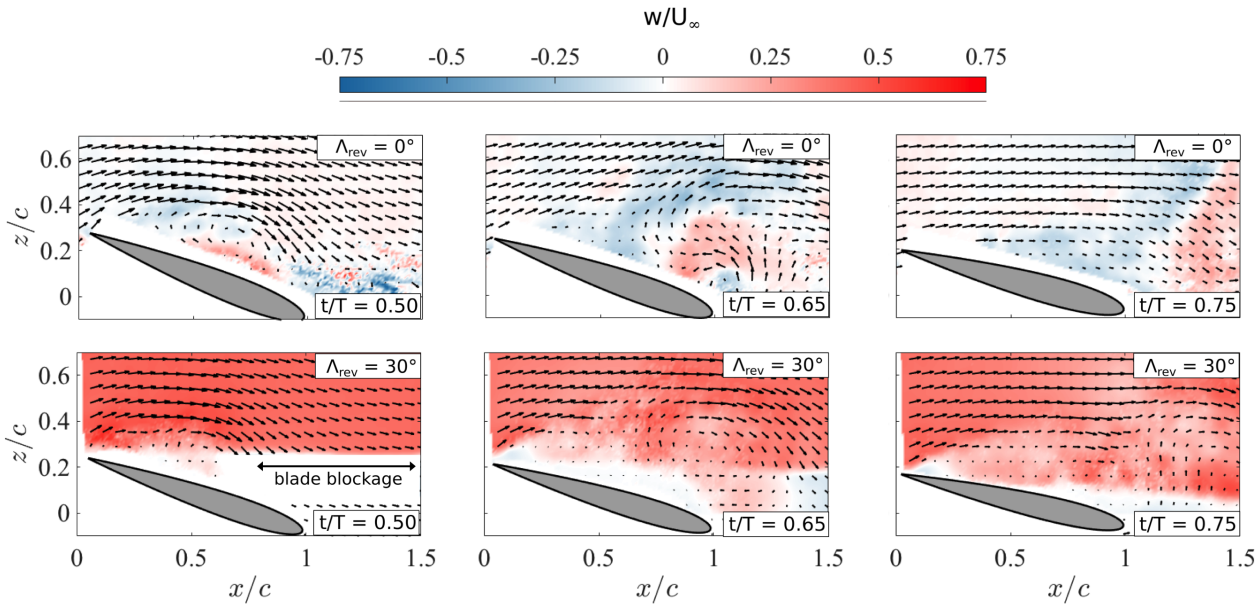

FIG. 19: Phase-averaged vector fields showing contours of spanwise flow for the unyawed (top) and yawed (bottom) conditions at $k = 0.217$. Red regions correspond to flow toward the tunnel floor (the expected direction), while blue represents flow toward the tunnel ceiling.

reduced frequency, the flowfield of the yawed blade shows only a strong RFDSV, while secondary flow structures are significantly weakened or absent. For $\Lambda_{\text{rev}} = 0°$, the surface pressure at $k = 0.160$ is dominated by two large local minima, corresponding to the RFDSV and the SDSV, but for $\Lambda_{\text{rev}} = 30°$, the surface pressure at $k = 0.160$ shows only a single, more sustained local minimum. These differences disappear at higher reduced frequency, $k = 0.450$, where no secondary flow structures are evident for $\Lambda_{\text{rev}} = 0°$ or $\Lambda_{\text{rev}} = 30°$.

- The suppression of secondary flow structures was consistent across multiple scalings of the blade pitch kinematics. Pressure measurements were repeated for alternate definitions of the reduced frequency and blade pitch angle, but the shedding pattern remained unchanged at $\Lambda_{rev} = 30°$.

- Both the unyawed and yawed configuration were subject to small spanwise gradients in the vorticity field, but the yawed configuration was found to have a significantly larger magnitude of spanwise flow. This spanwise flow magnifies the transport of vorticity, generated both at the leading and trailing edge, along the blade span. In light of the yawed blade's insensitivity to changes in kinematic scaling, the spanwise vorticity transport is believed to account for the suppression of secondary flow features at $\Lambda_{\text{rev}} = 30°$.

This experimental study lays the groundwork for a physical understanding of the three-dimensional behavior of the reverse flow dynamic stall vortex. Rotorcraft are subject to considerably higher spanwise flow gradients than the simple model considered here, suggesting that the spanwise transport of vorticity cannot necessarily be neglected when considering the behavior of the RFDSV on a spinning rotor. Coupled with results from full-scale and Mach-scale rotor tests, this work ultimately adds to the development of a predictive model for the impact of the reverse flow dynamic stall vortex on the aerodynamics of high advance ratio rotors.

VI. ACKNOWLEDGEMENTS

This work was supported by the U.S. Army/Navy/NASA Vertical Lift Research Center of Excellence Cooperative Agreement with Mahendra Bhagwat serving as Program Manager and Technical Agent, grant number W911W6-17-2-0004. The authors wish to acknowledge Jonathan Lefebvre, Peter Mancini, and Andrew Lind for their assistance throughout the wind-tunnel experiments.

VII. REFERENCES

[1] C.N.D. Bastian, L.V. Fulton, C.R. Mitchell, W. Pollard, D. Wiershem, and R. Wilson, "The future of vertical lift: Initial insights for aircraft capability and medical planning," Military Medicine **177**, 863–869 (2012).

[2] D. Ashby, W. Eadue, and G.J. Montoro, "An investigation of the reverse velocity rotor concept and its application to high speed rotorcraft," in *Biennial International Powered Lift Conference and Exhibit* (Williamsburg, Virginia, 2002) pp. 1–10.

[3] F D Harris, *Rotor Performance at High Advance Ratio*, NASA CR 215370 (2008).

[4] G. Bowen-Davies and I. Chopra, "Aeromechanics of a slowed rotor," Journal of the American Helicopter Society **60**, 1–13 (2015).

[5] J. Hodara and M.J. Smith, "Improvement of crossflow aerodynamic prediction for forward flight at all advance ratios," in *40th European Rotorcraft Forum* (2014) p. 114.

[6] A Datta, H Yeo, and T R Norman, "Experimental investigation and fundamental understanding of a full-scale slowed rotor at high advance ratio," Journal of the American Helicopter Society **58**, 1–17 (2013).

[7] B. Berry and I. Chopra, "Slowed rotor wind tunnel testing of an instrumented rotor at high advance ratio," in *40th European Rotorcraft Forum* (Southampton, England, 2014) p. 112.

[8] A. H. Lind and A. R. Jones, "Unsteady aerodynamics of reverse flow dynamic stall on an oscillating blade section," Physics of Fluids **28**, 122 (2016).

[9] L Smith, A H Lind, K Jacobson, Marilyn J Smith, and Anya R Jones, "Experimental and Computational Investigation of a Linearly Pitching NACA 0012 in Reverse Flow," in *72nd Forum of the AHS* (2016) p. 120.

[10] P. Purser and M. Spearman, *Wind-Tunnel Tests at Low Speed of Swept and Yawed Wings Having Various Plan Forms*, NACA TN 2445 (1951).

[11] R.E. Gormont, *A Mathematical Model of Unsteady Aerodynamics and Radial Flow for Application to Helicopter Rotors*, USAA MRDL 72-67 (1973).

[12] A. St Hilaire and F. Carta, *Analysis of Unswept and Swept Wing Chordwise Pressure Data from an Oscillating NACA0012 Experiment*, NASA CR 3567 (1983).

[13] P.F. Lorber, F.O. Carta, and A.F. Covino Jr, *An Oscillating Three-Dimensional Wing Experiment: Compressibility, Sweep, Rate, Waveform, and Geometry Effects on Unsteady Separation and Dynamic Stall*, UTRC R92-958325-6 (1992).

[14] J.G. Leishman, "Modeling sweep effects on dynamic stall," Journal of the American Helicopter Society **34**, 1829 (1989).

[15] T.T. Lim, C.J. Teo, K.B. Lua, and K.S. Yeo, "On the prolong attachment of leading edge vortex on a flapping wing," Modern Physics Letters B **23**, 357–360 (2009).

[16] J.G. Wong and D.E. Rival, "An investigation into vortex growth and stabilization for two-dimensional plunging and flapping plates with varying sweep," Journal of Fluids and Structures **43**, 231–243 (2013).

[17] L. Trollinger, X. Wang, and I. Chopra, "Refined measurement and validation of performance and loads of a mach-scaled rotor at high advance ratios," in *43rd European Rotorcraft Conference* (Milan, Italy, 2017) pp. 1–15.

[18] A H Lind, L N Trollinger, F H Manar, I Chopra, and A R Jones, "Flowfield measurements of reverse flow on a high advance ratio rotor," in *43rd European Rotorcraft Forum* (Milan, Italy, 2017) p. 115.

[19] L. Graftieaux, M. Michard, and N. Grosjean, "Combining piv, pod and vortex identification algorithms for the study of unsteady turbulent swirling flows," Measurement Science and Technology **12**, 1422–1429 (2001).

[20] J G Leishman, *Principles of Helicopter Aerodynamics*, 2nd ed. (Cambridge University Press, 2006).

[21] C.P. Ellington, C. van den Berg, A.P. Willmott, and A.L.R. Thomas, "Leading-edge vortices in insect flight," Nature **384**, 626–630 (1996).

[22] Albert Medina and Anya R. Jones, "Leading-edge vortex burst on a low aspect ratio rotating flat plate," Physical Review of Fluids **1**, 1–25 (2016).

[23] M.R. Visbal and D.J. Garmann, "Numerical investigation of spanwise end effects on dynamic stall of a pitching naca 0012 wing," in *55th AIAA Aerospace Sciences Meeting* (2017) pp. 1–22.